

Indentation of an elastic arch on a frictional substrate: Pinning, unfolding and snapping

Keisuke Yoshida and Hirofumi Wada

Department of Physical Sciences, Ritsumeikan University, Kusatsu, Shiga 525-8577, Japan

(Dated: November 21, 2023)

We investigate the morphology and mechanics of a naturally curved elastic arch loaded at its center and frictionally supported at both ends on a flat, rigid substrate. Through systematic numerical simulations, we classify the observed behaviors of the arch into three distinct types of configurations in terms of the arch geometry and the coefficient of static friction with the substrate. A linear theory is developed based on a planar elastica model combined with Amontons-Coulomb's frictional law, which quantitatively explains the numerically constructed phase diagram. The snapping transition of a loaded arch in a sufficiently large indentation regime, which involves a discontinuous force jump, is numerically observed. The proposed model problem allows a fully analytical investigation and demonstrates a rich variety of mechanical behaviors owing to the interplay between elasticity, geometry, and friction. This study provides a basis for understanding more common but complex systems, such as a cylindrical shell subjected to a concentrated load and simultaneously supported by frictional contact with surrounding objects.

I. INTRODUCTION

Designing the proper geometry of a thin structure is crucial for realizing its functionality and has become a central topic in the field of soft matter mechanics [1, 2]. For example, by choosing suitable geometrical and structural arrangements for the assembly of thin strips and harnessing their elastic forces, a variety of curved (pseudo) surfaces and their transformations have been achieved [3–5]. Typically, the fundamental set of building blocks for such advanced materials is intrinsically straight and/or uniformly curved rods, ribbons, and plates. In fact, it has been shown that the intrinsic curvature of a slender object introduces novel types of elastic instabilities and morphologies, which may find a variety of applications, such as mechanical metamaterials [6], jumping soft robotics [7, 8] and bio-inspired actuators [9].

Naturally, these geometrical structures are subjected to various boundary conditions depending on how they are mounted onto an entire physical system. In some cases, the relevant boundary conditions are not given a priori but rather in a state-dependent manner [10, 11]. For instance, when a wire is inserted into a narrow channel, it is resisted by the frictional forces exerted from the inner side of the wall [12, 13]. As the compressive force increases, the wire may buckle and eventually jam with undesired pressure applied to the wall [14–16], which is a potentially fatal problem in endoscopic surgery applications. Therefore, the morphologies of thin structures in contact with the surrounding objects or themselves have been extensively studied at various levels of complexity, ranging from the buckling of a single strip on a flat surface [17] to crumpled sheets in packing [18–23]. Notably, recent studies have also uncovered functional advantages of frictional contact, such as the force amplification in capstan problem [24, 25], elastic knots [26], interleaved plates [27, 28], and twisted yarn [29], as non-reciprocal mechanical responses in snap fits [30] and grasping [31]

and as energy absorption devices [32]. However, the interplay between natural curvature, elasticity, and contact mechanics, as well as the consequences of their potential applications, have not been fully explored.

To highlight the role of intrinsic geometry and frictional contact on the mechanics of a thin structure, we propose the investigation of the simplest possible system, an elastic arch on a rigid, flat frictional surface; see Fig. 1. Such a uniformly curved elastic strip can act as a leaf spring [33], exhibiting an intriguing mechanical response that is highly dependent on its configuration. In addition to its geometry-dominated nature, the arch can exhibit a rich variety of force responses against the indentation at its center when the friction acts to resist the tangential motion (i.e., slipping) of the two ends on the surface.

Most of the literature on the planar elastica prob-

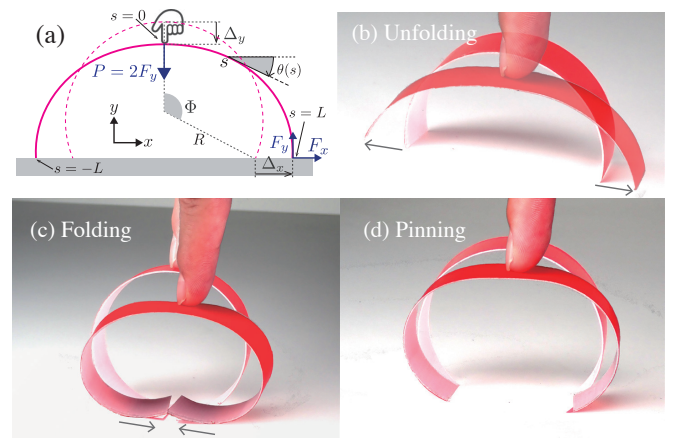


FIG. 1. Naturally curved elastic strip, which we call "arch", loaded at its center on a frictional substrate. (a) Definition of the coordinate system and variables in our theoretical analysis. (b)-(d) Photographs of the three characteristic configurations, i.e., unfolding, folding, and pinning, of a naturally curved plastic film ribbon, for illustration purposes only.

lem has focused on solving the nonlinear boundary value problem either analytically or numerically to address its large deformation behaviors. In this approach, we must deal with transcendental equations involving elliptical integrals [33–35]. As there are generally multiple solutions to these nonlinear equations, we must also identify which solution is the energy minimizer [36]. A uniform intrinsic curvature is equivalent to a premoment applied externally to an intrinsically straight elastica, making it difficult to find such a physical solution analytically [33]. Instead of employing a rigorous but implicit analytical approach that relies heavily on elliptic functions, we opt for a linear relationship between force and displacement in the curved elastica by focusing on a small amplitude deflection regime [12, 37, 38]. For example, the linear mechanical response of a curved elastic beam was previously examined to elucidate the climbing mechanism of gecko setae [39, 40].

In this study, we consider the indentation of an elastic arch placed on a friction substrate [Fig. 1 (a)]. We generalize the aforementioned small deflection theory to an intrinsically curved elastic strip within the framework of the planar elastica theory. The predictions of our analytical theory are corroborated by systematic numerical simulations.

The remainder of this paper is organized as follows: In Sec. II, numerical simulations are employed to investigate the deformation of an elastic arch loaded at its center on a frictional substrate [17, 30]. We identify three distinct behaviors, which we classify into folding, unfolding, and pinning phases, based on the static friction coefficient μ and the opening angle Φ of the arc (see Fig. 1 (a)). In Sec. III, we develop an analytical theory based on Kirchhoff’s elastic rod theory [41] combined with a dry friction law [42] and establish a linear response formula that quantitatively explains the mechanical phase diagram. In Sec. IV, we numerically address a variety of morphological transitions observed in the highly nonlinear deformation regime. In Sec. V, we summarize our main results and discuss potential avenues for further research.

II. NUMERICAL SIMULATION

A. Set up of the simulation

We consider the planar deformation of a uniform elastic arch of total length $2L$ and opening angle 2Φ . See Fig. 1 (a). In this study, we consider L and Φ as the basic geometric parameters, and the arch is assumed to have a uniform intrinsic curvature with a radius of curvature of $R = L/\Phi$. Gravity is ignored throughout the study.

The basic numerical method has been described previously [17, 30]. Therefore, several key aspects of our simulation method are briefly explained here. A continuous elastic arch is discretized into a chain of $N = 31 - 51$

nodes in which neighboring nodes are connected with sufficiently stiff springs of nearly constant length a . The force fields are calculated from properly defined stretching and bending elastic energies [17, 30]. The self-avoidance of the chain is taken into account by the repulsive potential, modeled as a harmonic potential with a sufficiently large modulus. Penetration of the chain into a flat rigid substrate is also prevented by the same type of potential. The tangential interaction of the chain nodes with the surface is modeled according to the Amon-ton–Coulomb law [42]. The position of each node evolves according to Newton’s equation of motion, with a small damping parameter that ensures numerical stability. We use the Euler iteration method to numerically integrate appropriately rescaled dynamical equations with a non-dimensional time step, which is typically 0.05. The output values are calculated every $10^5 - 10^6$ steps, and the total simulation time is $10^7 - 10^8$ steps.

In its initial configuration, the discretized arch is semi-circular in shape and located just above a rigid, flat substrate. We imposed a downward displacement at the center of the arc, Δ_y , and measured the reaction force P with increasing Δ_y quasi-statically. As soon as both ends of the arch come into contact with the surface, they move tangentially outward or inward [see Fig. 1(b) and 1(c), respectively] or remain stationary [Fig. 1(d)]. To classify the configurations of the arch quantitatively, we measure the resulting outward horizontal displacement, Δ_x , and define “unfolding” for $\Delta_x > 0$, “pinning” for $\Delta_x = 0$, and “folding” for $\Delta_x < 0$, respectively. To establish a mechanical phase diagram, we explore a wide range of parameter spaces (Φ, μ) : $\Phi = 20^\circ - 178^\circ$ and $\mu = 0.1 - 1.2$.

B. Results

The results of the systematic numerical investigation are presented in Fig. 2 (a). We observe three distinct mechanical phases depending on the parameters (Φ, μ) .

We first focus on the frictionless case ($\mu = 0$) shown in Fig. 2(a). For a shallow arch ($\Phi < \Phi_c$), where Φ_c is determined as follows, the two ends slip outward ($\Delta_x > 0$) as soon as the arch is loaded at its center. We define this phase as “unfolding.” A typical force vs. displacement curve for the unfolding phase is shown in Fig. 2(b) (i). For a low force regime, the force increases linearly with the vertical displacement $\Delta_y (\ll L)$. With increasing vertical displacement, the force increased but deviated from the linear slope, whereas the two ends continued to slip outwards [Fig. 2(b-i) and Fig. 2(c-i)].

In contrast, for a deep arch, i.e., $\Phi > \Phi_c$, the two ends initially slip inward ($\Delta_x < 0$); we define this phase as “folding.” The force in the folding phase also initially exhibits a linear increase with vertical displacement but then increased rapidly because of self-avoiding interactions [Fig. 2(b-iii) and 2(c-iii)]. The boundary between the folding and unfolding phases is $\Phi_c \approx 142^\circ$ for

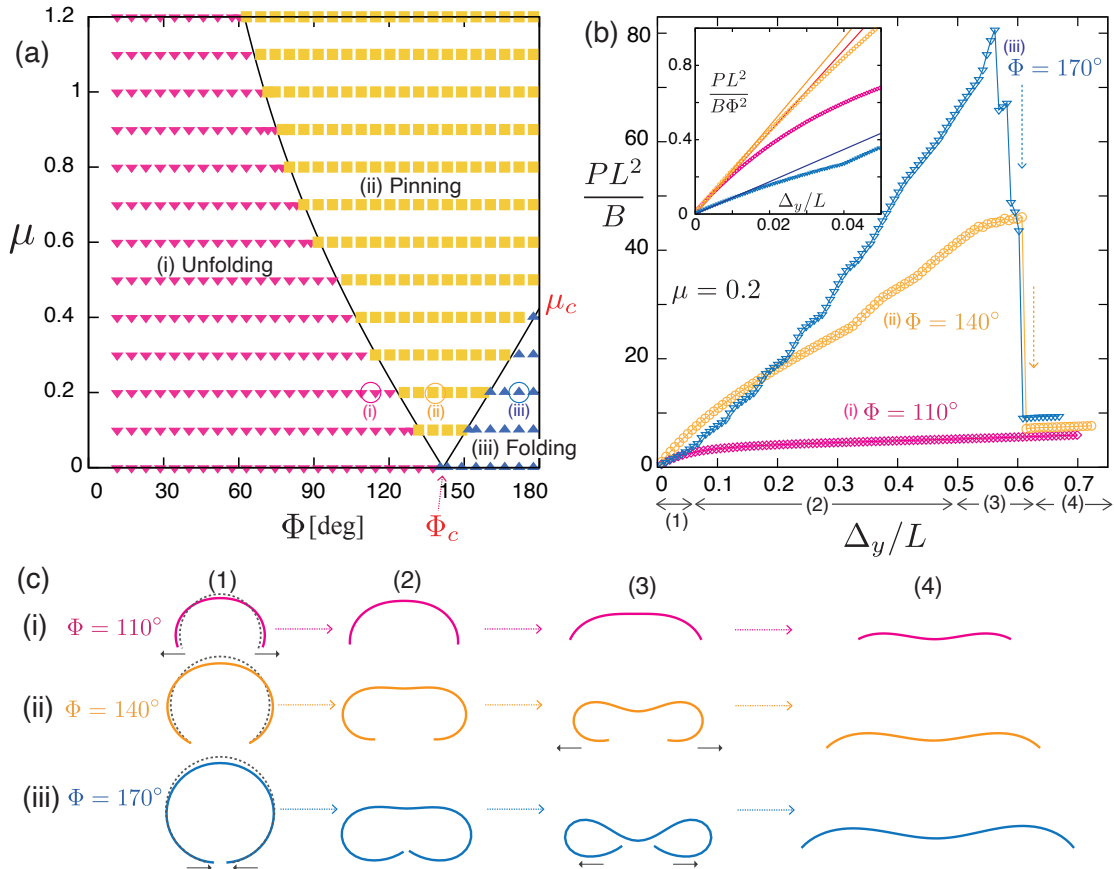


FIG. 2. Phase diagram, representative force-displacement curves, and configurations. (a) Numerically constructed phase diagram of the (Φ, μ) space. The pink, yellow, and blue symbols represent the (i) unfolding, (ii) pinning, and (iii) folding phases, respectively. Solid lines represent our analytical predictions; see the main text. (b) Rescaled indentation force PL^2/B as a function of the rescaled vertical displacement at the arch’s center, Δ_y/L , for $\mu = 0.2$. The inset displays the same data focusing on the small indentation regime, $\Delta_y/L < 0.05$. Note that the vertical axis in the inset shows $PL^2/B\Phi^2$ because our linear theory is developed under the basic assumption given by $PL^2/(B\Phi^2) \ll 1$ (see the main text). (c) Representative snapshots of an arch for increasing Δ_y/L , obtained from the numerical simulations; (1)-(4) correspond to those shown in the horizontal axis in (b). Corresponding locations of (i)-(iii) on the phase diagram are also shown in (a).

$\mu = 0$. In addition, the folding phase disappears when $\mu > \mu_c \approx 0.42$. In the next section, we develop an analytical argument to corroborate these numerical findings and show that Φ_c and μ_c are, in fact, universal numbers in the sense that they are independent of any material parameters, such as Young’s modulus of the arch.

Next, when frictional interactions occur between the arch and the substrate ($\mu > 0$), the phase diagram bifurcates, resulting in the emergence of the third phase, which we have defined as “pinning.” In the pinning phase, both ends of the arch remain immobile during the indentation. In Fig. 2(a), the pinning phase expands as μ increases and prevails in the diagram for sufficiently large friction. The diagram is constructed based on the response of the arch in the low-force regime. In the pin-

ning phase, the two ends are maintained pinned (i.e., $\Delta_x = 0$) until the arch is strongly squeezed [Fig. 2(b-ii) and 2(c-ii)]. At some point, the two ends suddenly snap outwards, and the loading force P decreases discontinuously to forces of the same magnitude as those in the unfolding phase [See Fig. 2(b-ii)].

III. THEORETICAL ANALYSIS

A. Set up of the analysis

Focusing on the linear regime characterized by a sufficiently small vertical displacement $\Delta_y \ll L$, we rationalize the above numerical findings in the framework of the

inextensible planar elastica theory [33, 41]. In the two-dimensional problem, the position of the centerline of the arch is represented as $\mathbf{r}(s) = (x(s), y(s))$, where s is defined as the arc length parameter $s \in [-L, L]$. We assume that the center of the arch is at $s = 0$, with the left and right ends at $s = -L$ and L , respectively. In addition to the Cartesian coordinate representation, we define the variable $\theta(s)$ representing the angle between the tangent line at s and the horizontal axis that is suitable for considering the inextensibility conditions implied in the elastica model. From Fig. 1 (a), we find $dx(s)/ds = \cos \theta(s)$ and $dy(s)/ds = -\sin \theta(s)$. Assuming a symmetric deflection of the arch about $s = 0$ as observed in our numerical simulations, we consider the deformation of only half of the arch, that is, the segment $0 \leq s \leq L$. This implies that the arch at $s = 0$ is being clamped horizontally; that is, $\theta(0) = 0$.

A simple geometric consideration indicates the following relationships:

$$\int_0^L \cos \theta(s) ds = \frac{\sin \Phi}{\Phi} L + \Delta_x, \quad (1)$$

$$\int_0^L \sin \theta(s) ds = \frac{1 - \cos \Phi}{\Phi} L - \Delta_y. \quad (2)$$

When a concentrated downward force P is applied at $s = 0$, the substrate exerts a reaction force (F_x, F_y) on the (right) edge ($s = L$). The overall vertical force balance is $P = 2F_y$. The elastica equilibrium equation [33, 41] is given by

$$B\theta''(s) - F_x \sin \theta(s) - F_y \cos \theta(s) = 0, \quad (3)$$

where the prime symbol ($'$) represents the derivative with respect to s , and B is the bending modulus. In addition, we assume moment-free boundary conditions at both ends [17, 30], implying $\theta'(L) = \Phi/L$. We also assume that there is no inflection point in the shape of our elastica considered here. Integrating Eq. (3) using the boundary conditions at $s = L$ given above, we find that

$$\frac{ds}{L} = \frac{d\theta}{\Phi} \left[1 + \frac{2}{\Phi^2} \begin{pmatrix} f_x \\ f_y \end{pmatrix} \cdot \begin{pmatrix} -\cos \theta + \cos \theta(L) \\ \sin \theta - \sin \theta(L) \end{pmatrix} \right]^{-1/2}, \quad (4)$$

where we define the nondimensional force as

$$f_\alpha = \frac{F_\alpha L^2}{B}, \quad (5)$$

for $\alpha = x, y$. Equation (4) can be integrated exactly using elliptic integrals, but it is notoriously cumbersome for naturally curved beams [33]. Instead, focusing on a low force regime characterized by $f_\alpha/\Phi^2 \ll 1$ for $\alpha = x$ and y , we linearize Eq. (4) and obtain

$$\frac{ds}{L} \approx \frac{d\theta}{\Phi} \left[1 - \frac{1}{\Phi^2} \begin{pmatrix} f_x \\ f_y \end{pmatrix} \cdot \begin{pmatrix} -\cos \theta + \cos \theta(L) \\ \sin \theta - \sin \theta(L) \end{pmatrix} \right]. \quad (6)$$

By applying the integrals in Eqs. (1) and (2) using Eq. (6) and the condition of inextensibility, we arrive at a linear relationship given by

$$\frac{\Delta_\alpha}{L} = C_{\alpha\beta} \frac{F_\beta L^2}{B}, \quad (7)$$

where the Greek indices run in the x and y directions for which Einstein's sum rule is implied. The symmetric compliance matrix $C_{\alpha\beta}$ in Eq. (7) is defined as

$$C_{xx}(\Phi) = \frac{1}{2\Phi^2} - \frac{\cos \Phi}{\Phi^3} \left(\frac{3}{2} \sin \Phi - \Phi \cos \Phi \right), \quad (8)$$

$$C_{xy}(\Phi) = \frac{1}{2\Phi^3} + \frac{\cos \Phi}{\Phi^3} \left(1 - \frac{3}{2} \cos \Phi - \Phi \sin \Phi \right), \quad (9)$$

$$C_{yx}(\Phi) = C_{xy}(\Phi), \quad (10)$$

$$C_{yy}(\Phi) = \frac{1}{2\Phi^2} + \frac{\sin \Phi}{\Phi^3} \left(-2 + \frac{3}{2} \cos \Phi + \Phi \sin \Phi \right). \quad (11)$$

The inverse of matrix \mathbf{C} , which we write as \mathbf{C}^{-1} , is the (non-dimensional) rigidity matrix that can be determined from Φ only. Note that the off-diagonal elements of \mathbf{C} provide the normal tangential coupling, which quantifies the lateral displacement induced by the vertical loading force.

B. Effective stiffness of the arch

To characterize the mechanical properties of the elastic arch on a flat substrate, we derive Hooke's law for indentation as follows:

$$\frac{PL^2}{B} = K(\Phi) \frac{\Delta_y}{L}, \quad (12)$$

where $K(\Phi)$ denotes the dimensionless effective stiffness. A specific form of $K(\Phi)$ can be obtained analytically by using Eq. (7) once the lateral force F_x is determined by the given boundary conditions. To encompass the different conditions imposed along the x direction, we first assume a simple but general boundary condition in which the end positions of the arch are constrained by linear springs with a dimensionless stiffness k ; that is,

$$\frac{F_x L^2}{B} = -k \frac{\Delta_x}{L}. \quad (13)$$

For $k = 0$, the elastic strip is free to move horizontally (on a frictionless substrate), whereas for $k \rightarrow \infty$, the ends are firmly fixed at their initial positions. Substituting Eq. (13) into Eq. (7), we obtain

$$K_{\text{el}}(\Phi, k) = K_{\text{pin}}(\Phi) \frac{k + (C_{xx})^{-1}}{k + (C^{-1})_{xx}}, \quad (14)$$

where

$$K_{\text{pin}}(\Phi) = 2(C^{-1})_{yy}. \quad (15)$$

We define $(C^{-1})_{\alpha\beta}$ as the (α, β) component of the inverse matrix \mathbf{C}^{-1} and $(C_{\alpha\beta})^{-1} = 1/C_{\alpha\beta}$. It should be noted that $K_{\text{pin}}(\Phi) = \lim_{k \rightarrow \infty} K_{\text{el}}(\Phi, k)$ represents the stiffness of the pinning boundary conditions. In Fig. 3 (a), we plot $K_{\text{el}}/K_{\text{pin}}$ as a function of Φ for various values of k (as indicated in the legend of Fig. 3 (b)). A shallow strip ($\Phi \ll 1$) behaves much softer for a finite k compared to the pinning case ($k = \infty$). In particular, we find

$$\lim_{\Phi \rightarrow 0} \frac{K_{\text{el}}(\Phi, 0)}{K_{\text{el}}(\Phi, \infty)} = \frac{3}{128}. \quad (16)$$

The relationship between the lateral and vertical displacements can also be obtained as

$$\frac{\Delta_x}{\Delta_y} = -\frac{(C^{-1})_{xy}}{k + (C^{-1})_{xx}}, \quad (17)$$

and are plotted in Fig. 3 (b). An indentation, that is, an increase in Δ_y , induces lateral displacement Δ_x , and the magnitude of this coupling depends on the intrinsic curvature Φ . As seen in Figs. 3 (a) and (b), we have $K_{\text{el}}/K_{\text{pin}} = 1$ at $\Phi = \Phi_c$ irrespective of the value of k , at which $|\Delta_x/\Delta_y| = 0$. Thus, Φ_c is determined by solving $(C^{-1})_{xy}(\Phi) = 0$ numerically, from which we find $\Phi_c \approx 142^\circ$. For $\Phi = \Phi_c$, the ends of the arch are virtually pinned, irrespective of the value of k , which is thus purely geometric. Note also that Eq. (17) predicts the unfolding ($\Delta_x > 0$) and folding ($\Delta_x < 0$) phases for shallow ($\Phi < \Phi_c$) and deep ($\Phi > \Phi_c$) arches, respectively (see Fig. 3 (b)), which agrees with the diagram shown in Fig. 2 (a). Considering that the present analytical argument applies to any frictionless ($\mu = 0$) substrate, we fully explain the threshold angle Φ_c observed in the diagram given in Fig. 2.

To rationalize the numerically constructed diagram shown in Fig. 2, we now consider frictional interactions with the substrate, assuming the Amontons-Coulomb friction law. Based on the classification shown in Fig. 2, the stiffness $K(\Phi)$ differs between the three phases. The stiffness of the pinning phase has been discussed above (See Eq. (15)). In the unfolding and folding phases, the quasi-static loading assumption implies the critical condition $|F_x/F_y| = \mu$. Combining this with Eq. (7), we obtain:

$$K_{\pm}(\Phi, \mu) = K_{\text{pin}} \frac{(C_{xx})^{-1}}{(C^{-1})_{xx} \pm \mu(C^{-1})_{xy}}, \quad (18)$$

where the positive and negative indices in K_{\pm} represent the unfolded and folded phases, respectively. Note that Eq. (18) with $\mu = 0$ agrees with Eq. (14), where $k = 0$. In the inset of Fig. 2 (b), we plot the force law based on Eqs. (15) and (18) and observe consistency with our simulation results.

C. Phase boundaries

Using the aforementioned theoretical framework, we analytically determine the phase boundaries, as shown

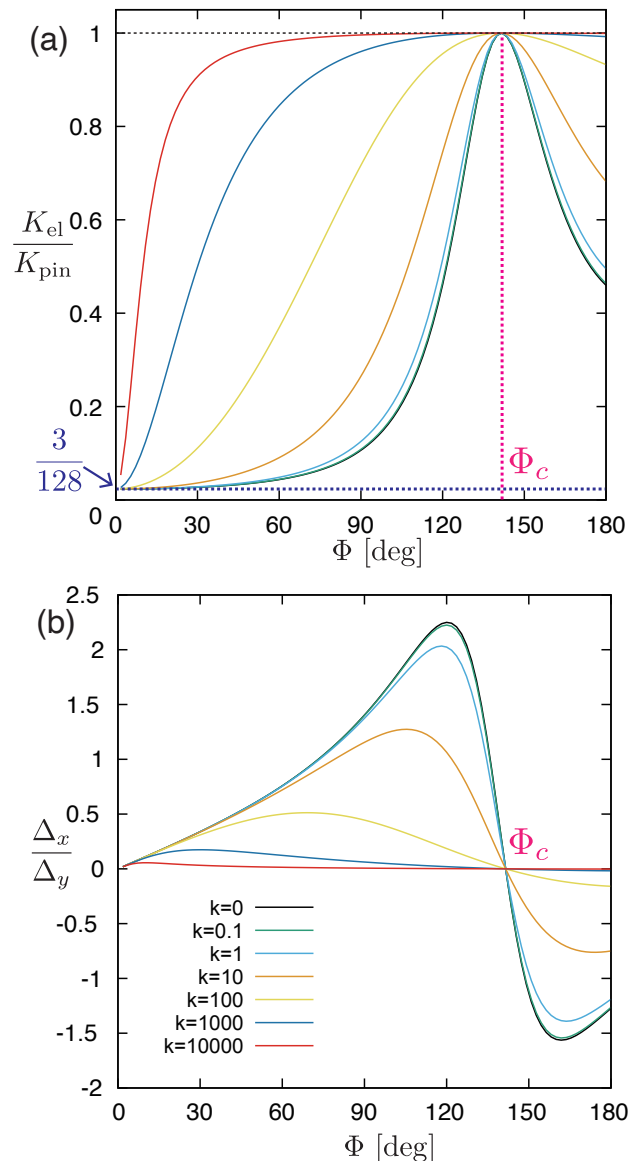


FIG. 3. Analytical results of our linear theory for various values of the boundary stiffness k . (a) Normalized effective stiffness $K_{\text{el}}/K_{\text{pin}}$ plotted as a function of the opening angle Φ for various k [indicated in the legend of (b)], based on Eq. (14). (b) Ratio of the vertical (Δ_y) to horizontal (Δ_x) displacement plotted as a function of Φ for various k (indicated in the legend), based on Eq. (17).

in Fig. 2 (a). First, we consider an elastic arch in the pinning configuration. By substituting $\Delta_x = 0$ into Eq. (7), we immediately obtain $F_x/F_y = -C_{xy}/C_{xx}$. The critical condition $\mu = |F_x/F_y|$ is satisfied for the two-phase boundary lines shown in Fig. 2 (a). As it is easy to see that $C_{xy} > 0$ for $\Phi < \Phi_c$, the pinning-unfolding boundary line is determined by

$$\mu = \frac{C_{xy}}{C_{xx}}. \quad (19)$$

Similarly, because $C_{xy} < 0$ for $\Phi > \Phi_c$, the pinning-folding boundary line was determined as follows:

$$\mu = -\frac{C_{xy}}{C_{xx}}. \quad (20)$$

We plot Eqs.(19) and (20) in Fig. 2 (a), which are in excellent agreement with the simulation results. The critical value of the static friction coefficient μ_c , above which the folding phase disappears for all Φ values, is directly obtained from Eq. (20) as

$$\mu_c = -\frac{C_{xy}(180^\circ)}{C_{xx}(180^\circ)} = \frac{4}{3\pi} \approx 0.424, \quad (21)$$

which is in quantitative agreement with the numerical results shown in Fig. 2 (a). We have then established the two critical parameters, Φ_c and μ_c , which are essentially independent of elastic properties such as Young's modulus; hence, they are purely geometric. Note that Eq. (19) asymptotically approaches $25/(16\Phi)$ for $\Phi \ll 1$, indicating that the unfolding region decreases as μ increases but remains for an arbitrarily large value of μ .

IV. LARGE INDENTATIONS

When the loading displacement is sufficiently large, the mechanical response significantly changes. Figure 4(a) shows a typical force-displacement curve obtained from our numerical simulation. As discussed in Sec. II B, for $(\Phi, \mu) = (110^\circ, 0.2)$, the curved strip unfolds upon indentation at its center, and as the displacement increases, the loading force increases more slowly than its initial linear response slope. To understand the characteristic force behavior in terms of the strip configuration, we plot $|F_x/F_y|$ as a function of Δ_y/L in Fig. 4(b). For $\mu = 0.2$ (red symbols), the strip undergoes quasi-static slipping because $|F_x/F_y| \simeq \mu$ holds in Fig. 4(b)). In contrast, for $(\Phi, \mu) = (110^\circ, 0.4)$ (blue symbols), the strip are initially pinned as $|F_x/F_y| < \mu$ for a small Δ_y/L . In fact, Eq. (19) predicts $|F_x/F_y| = C_{xy}(110^\circ)/C_{xx}(110^\circ) \approx 0.36 < \mu (= 0.4)$, which is consistent with the numerical results shown in Fig. 4(b). Although our linear theory predicts that $|F_x/F_y|$ is independent of Δ_y , beyond this linear regime, $|F_x/F_y|$ is actually observed to increase with increasing Δ_y/L . As soon as $|F_x/F_y| = \mu (= 0.4$ in the present case), the strip ends snap outward and the force drops discontinuously, as shown in Figs. 4(a) and 2(b-ii). Beyond this transition point, the critical condition $|F_x/F_y| \approx \mu$ holds for increasing Δ_y/L , whereas the magnitude of the force is found to be of the same order as that for $\mu = 0.2$ (Fig. 4(a)). For comparison, we numerically investigate an elastic arch firmly pinned at its two ends and loaded at its center. As seen in Fig. 4 (a), the force-displacement curve is in excellent agreement with that for $\mu = 0.4$ provided that $|F_x/F_y| < \mu$. Therefore, the critical displacement for the pinning-to-slipping transition (accompanying snapping) can be precisely predicted using this comparison.

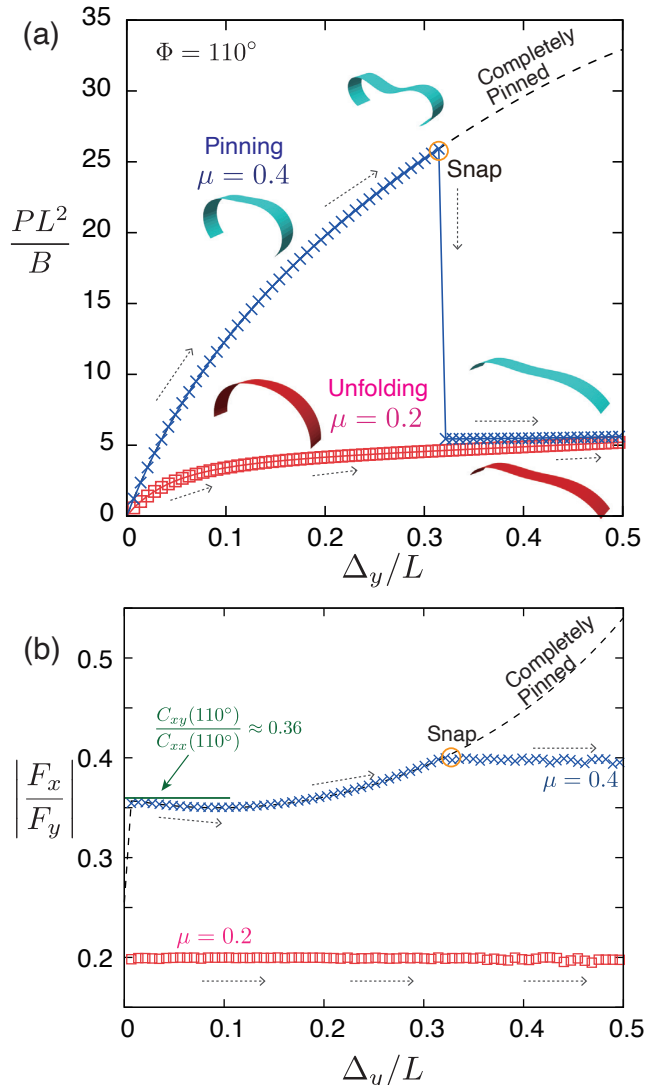


FIG. 4. Snapping behavior and underlying friction mechanism along with the arch configurations. (a) Rescaled indentation force PL^2/B plotted as a function of the rescaled vertical displacement Δ_y/L for $\Phi = 110^\circ$ and for $\mu = 0.2$ (red, unfolding) and $\mu = 0.4$ (blue, pinning). The insets show the several representative configurations from the numerical simulations. (b) Plot of $|F_x/F_y|$ as a function of Δ_y/L for the two cases shown in (a). The snap point indicated on the data for $\mu = 0.4$ correspond to the snap point of the significant force drop in (a). The dotted line is the prediction for the hinge-hinge (i.e., "completely pinned") boundary condition.

V. DISCUSSION AND CONCLUSION

By combining numerical simulations and analytical theory, we have quantified the mechanical responses of an elastic arch loaded at its center and supported frictionally at both ends on a flat substrate. We have formulated the compliance matrix of the arch against indentation, which is essentially a function of the intrinsic geometry

of the arch only. When combined with specific boundary conditions, this allows us to obtain an effective Hooke's law. Our theoretical framework quantitatively predicts the numerically constructed phase diagram.

We have also numerically investigated the deformation behavior of the arch at large indentations. The arch exhibited a snapping shape transition, which could not be captured by our linear response analysis. We have also shown that the force drastically decreases during the snapping transition, which is potentially useful in the application of efficient energy-absorbing materials [32, 43, 44].

This study has several possible extensions. First, the configuration of a naturally curved elastica is mathematically equivalent to the so-called "sticky elastica" problem [45]. Sticky elastica refers to the delaminated configuration of an elastic strip that is initially adhered to a wet substrate or liquid surface. In this setup, the ends of the strip must satisfy the boundary condition $\theta' \propto 1/\ell_{ec}$, where ℓ_{ec} is often termed as "elasto-capillary length" [46]. Therefore, our theoretical framework may be applicable to the quantitative estimation of the adhesion energy of an elastic sheet or strip on a sticky surface [46, 47].

Second, extending our study to thin-shell mechanics is clearly an interesting but challenging endeavor. The indentation behavior of a semi-cylindrical shell has been extensively studied previously, usually under clamped boundary conditions for lengthwise edges where the remaining two edges are free. The localized deformation of a cylindrical shell is inevitably accompanied by in-plane

stretching [2, 41], leading to stress focusing and the creation of a pair of defects [20, 48]. These individual structures can migrate to the free edges, where they disappear, to reduce the stretching energy, and the indentation force decreases drastically. At this point, the shell recovers its isometrically deformed shape, similar to the M-shape observed in the planar elastica model [48, 49]. How such generic behavior is modified if the edges of the shell are supported by frictional interactions with a flat substrate is an intriguing problem that needs to be investigated.

Finally, the theoretical findings must be verified through physical experiments. Throughout the study, we assumed symmetric deformation of an ideal arch with a uniform natural curvature and elastic modulus. However, our preliminary experiments suggest that the validity of these simplified assumptions may have to be examined because of the limitations in the fabrication of a physical experimental model. In experiments, the arch is often observed to undergo asymmetric buckling deformation upon indentation at its center. Further theoretical investigation of such asymmetric deformation modes, along with quantitative experimental verification, is required to understand the complex mechanical responses of curved elastic structures supported by a frictional substrate.

ACKNOWLEDGMENTS

Financial support from JSPS KAKENHI (Grant Nos. 22H05067 and 22H01192 to HW), a Grant-in-Aid for JSPS Research Fellows (DC1, No. 21J22837 to KY), and the Sasakawa Scientific Research Grant from the Japan Science Society (No.2020-2005 to KY) is acknowledged.

-
- [1] D. Vella, Buffering by buckling as a route for elastic deformation, *Nature Reviews Physics* **1**, 425 (2019).
- [2] D. P. Holmes, Elasticity and stability of shape-shifting structures, *Curr. Opin. Colloid In.* **40**, 118 (2019).
- [3] M. Liu, L. Domino, and D. Vella, Tapered elasticae as a route for axisymmetric morphing structures, *Soft Matter* **16**, 7739 (2020).
- [4] C. Baek, A. G. Martin, S. Poincloux, T. Chen, and P. M. Reis, Smooth triaxial weaving with naturally curved ribbons, *Phys. Rev. Lett.* **127**, 104301 (2021).
- [5] T. J. Jones, T. Dupuis, E. Jambon-Puillet, J. Marthelot, and P.-T. Brun, Soft deployable structures via core-shell inflatables, *Phys. Rev. Lett.* **130**, 128201 (2023).
- [6] K. Bertoldi, V. Vitelli, J. Christensen, and M. Van Hecke, Flexible mechanical metamaterials, *Nat. Rev. Mater.* **2**, 1 (2017).
- [7] D. Rus and M. T. Tolley, Design, fabrication and control of soft robots, *Nature* **521**, 467 (2015).
- [8] S. Chen, Y. Cao, M. Sarparast, H. Yuan, L. Dong, X. Tan, and C. Cao, Soft crawling robots: design, actuation, and locomotion, *Adv. Mater. Technol.* **5**, 1900837 (2020).
- [9] S. Wei and T. K. Ghosh, Bioinspired structures for soft actuators, *Adv. Mater. Technol.* **7**, 2101521 (2022).
- [10] D. Bigoni, F. Dal Corso, F. Bosi, and D. Misseroni, Eshelby-like forces acting on elastic structures: Theoretical and experimental proof, *Mech. Mater.* **80**, 368 (2015), *materials and Interfaces*.
- [11] D. Bigoni, F. Bosi, F. Dal Corso, and D. Misseroni, Configurational forces on elastic structures, in *50+ Years of AIMETA*, edited by G. Rega (Springer International Publishing, Cham, 2022) pp. 229–241.
- [12] R. C. Benson, Stick/Slip Conditions for a Thin, Incomplete, Elastic Ring Impinging on a Frictional Barrier, *J. Appl. Mech.* **49**, 231 (1982).
- [13] C.-W. Liu and J.-S. Chen, Effect of coulomb friction on the deformation of an elastica constrained in a straight channel with clearance, *Eur. J. Mech. A-Solid.* **39**, 50 (2013).
- [14] R. H. Plaut, S. Suherman, D. A. Dillard, B. E. Williams, and L. T. Watson, Deflections and buckling of a bent elastica in contact with a flat surface, *Int. J. Solids Struct.* **36**, 1209 (1999).
- [15] B. Roman and A. Pocheau, Postbuckling of bilaterally constrained rectangular thin plates, *J. Mech. Phys. Solids* **50**, 2379 (2002).
- [16] H. Chai, On the post-buckling behavior of bilaterally constrained plates, *Int. J. Solids Struct.* **39**, 2911 (2002).
- [17] T. G. Sano, T. Yamaguchi, and H. Wada, Slip morphology of elastic strips on frictional rigid substrates, *Phys.*

- Rev. Lett. **118**, 178001 (2017).
- [18] C. Donato, M. Gomes, and R. de Souza, Scaling properties in the packing of crumpled wires, Phys. Rev. E **67**, 026110 (2003).
- [19] L. Boué, M. Adda-Bedia, A. Boudaoud, D. Cassani, Y. Couder, A. Eddi, and M. Trejo, Spiral patterns in the packing of flexible structures, Phys. Rev. Lett. **97**, 166104 (2006).
- [20] T. A. Witten, Stress focusing in elastic sheets, Rev. Mod. Phys. **79**, 643 (2007).
- [21] E. Cerda and L. Mahadevan, Conical surfaces and crescent singularities in crumpled sheets, Phys. Rev. Lett. **80**, 2358 (1998).
- [22] N. Stoop, F. K. Wittel, and H. J. Herrmann, Morphological phases of crumpled wire, Phys. Rev. Lett. **101**, 094101 (2008).
- [23] S. Alben, Packing of elastic rings with friction, P. R. Soc. A **478**, 20210742 (2022).
- [24] S. Ghosal, Capstan friction model for dna ejection from bacteriophages, Phys. Rev. Lett. **109**, 248105 (2012).
- [25] P. Grandgeorge, T. G. Sano, and P. M. Reis, An elastic rod in frictional contact with a rigid cylinder, J. Mech. Phys. Solids **164**, 104885 (2022).
- [26] B. Audoly, N. Clauvelin, and S. Neukirch, Elastic knots, Phys. Rev. Lett. **99**, 164301 (2007).
- [27] H. Alarcón, T. Salez, C. Poulard, J.-F. Bloch, E. Raphaël, K. Dalnoki-Veress, and F. Restagno, Self-amplification of solid friction in interleaved assemblies, Phys. Rev. Lett. **116**, 015502 (2016).
- [28] S. Poincloux, T. Chen, B. Audoly, and P. M. Reis, Bending response of a book with internal friction, Phys. Rev. Lett. **126**, 218004 (2021).
- [29] A. Seguin and J. Crassous, Twist-controlled force amplification and spinning tension transition in yarn, Phys. Rev. Lett. **128**, 078002 (2022).
- [30] K. Yoshida and H. Wada, Mechanics of a snap fit, Phys. Rev. Lett. **125**, 194301 (2020).
- [31] Y. Yang, K. Vella, and D. P. Holmes, Grasping with kirigami shells, Sci. Robot. **6**, eabd6426 (2021).
- [32] K. Fu, Z. Zhao, and L. Jin, Programmable granular metamaterials for reusable energy absorption, Adv. Functional Materials **29**, 1901258 (2019).
- [33] R. Frisch-Fay, *Flexible bars* (Butterworths, 1962).
- [34] R. Nordgren, On finite deflection of an extensible circular ring segment, Int. J. Solids Struct. **2**, 223 (1966).
- [35] R. C. Benson, The Deformation of a Thin, Incomplete, Elastic Ring in a Frictional Channel, J. Appl. Mech. **48**, 895 (1981).
- [36] P. Patricio, M. Adda-Bedia, and M. B. Amar, An elastica problem: instabilities of an elastic arch, Physica **124**, 285 (1998).
- [37] H. D. Conway, The Nonlinear Bending of Thin Circular Rods, J. Appl. Mech. **23**, 7 (2021).
- [38] S. P. Timoshenko and J. M. Gere, *Theory of elastic stability* (Courier Corporation, 2009).
- [39] T. Yamaguchi, N. Gravish, K. Autumn, and C. Creton, Microscopic modeling of the dynamics of frictional adhesion in the gecko attachment system, J. Phys. Chem. B **113**, 3622 (2009).
- [40] B. Zhao, N. Pesika, H. Zeng, Z. Wei, Y. Chen, K. Autumn, K. Turner, and J. Israelachvili, Role of tilted adhesion fibrils (setae) in the adhesion and locomotion of gecko-like systems, J. Phys. Chem. B **113**, 3615 (2009).
- [41] B. Audoly and Y. Pomeau, *Elasticity and geometry: from hair curls to the non-linear response of shells* (Oxford university press, 2010).
- [42] V. L. Popov, *Contact mechanics and friction* (Springer, 2010).
- [43] A. P. Garland, K. M. Adstedt, Z. J. Casias, B. C. White, W. M. Mook, B. Kaehr, B. H. Jared, B. T. Lester, N. S. Leathe, E. Schwaller, *et al.*, Coulombic friction in metamaterials to dissipate mechanical energy, Extreme Mech. Lett. **40**, 100847 (2020).
- [44] T. G. Sano, E. Hohnadel, T. Kawata, T. Métivet, and F. Bertails-Descoubes, Randomly stacked open cylindrical shells as functional mechanical energy absorber, Commun. Mater. **4**, 59 (2023).
- [45] T. J. Wagner and D. Vella, The ‘sticky elastica’: delamination blisters beyond small deformations, Soft Matter **9**, 1025 (2013).
- [46] B. Roman and J. Bico, Elasto-capillarity: deforming an elastic structure with a liquid droplet, J. Phys-Condens Mat. **22**, 493101 (2010).
- [47] T. Elder, T. Twohig, H. Singh, and A. B. Croll, Adhesion of a tape loop, Soft Matter **16**, 10611 (2020).
- [48] A. Vaziri and L. Mahadevan, Localized and extended deformations of elastic shells, Proc. Natl. Acad. Sci. USA **105**, 7913 (2008).
- [49] A. Boudaoud, P. Patricio, Y. Couder, and M. Ben Amar, Dynamics of singularities in a constrained elastic plate, Nature **407**, 718 (2000).